DOI: 10.21062/mft.2025.060 © 2025 Manufacturing Technology. All rights reserved. http://www.journalmt.com

Strain Field Determination for Additively Manufactured Thermoplastics Using Computer Vision

Jaroslav Majko (0000-0001-7136-2656)¹, Ondrej Piroh (0009-0003-6939-2188)¹, Ján Minárik (0009-0000-7863-4263)¹, Milan Vaško (0000-0003-3585-2572)¹, Marián Handrik (0000-0002-8622-3103)¹, Milan Sága (0000-0002-0938-8772)¹, Zbigniew Saternus (0000-0002-3837-1072)²

¹Department of Applied Mechanics, Faculty of Mechanical Engineering, University of Žilina. Univerzitná 8215/1, 010 26 Žilina. Slovak Republic. E-mail: jaroslav.majko@fstroj.uniza.sk; Ondrej.piroh@fstroj.uniza.sk; jan.minarik@fstroj.uniza.sk; milan.vasko@fstroj.uniza.sk; marian.handrik@fstroj.uniza.sk; milan.saga@fstroj.uniza.sk ²Faculty of Mechanical Engineering and Computer Science, Czestochowa University of Technology, Dabrowskiego 69, 42-201 Czestochowa, Poland. E-mail: zbigniew.saternus@pcz.pl

The effective application of additively manufactured materials requires accurate identification of their mechanical properties as well as damage mechanisms. Computer vision offers a novel approach for noncontact measurements, enabling the identification of selected mechanical properties. This paper presents a new method based on image analysis and the detection of circular markers for non-contact displacement measurements. The core principle involves detecting the centers of gravity of the circular markers formed on the sample under investigation. The centers of gravity are evaluated on each image created during the tensile test, representing nodal points. At these points, displacements are determined based on the non-contact extensometer. The deformations sought are a function of the displacements at each nodal point. These values were calculated based on several theoretical models, also used in the finite element analysis. The paper describes the computational procedure for determining the deformations based on the mentioned theoretical models. Subsequently, the total strain field is determined using linear interpolation of the displacement values at the individual nodal points. The results provided by each of the theoretical models were compared.

Keywords: FFF, Object boundary detection, Infinitesimal strain tensor, Lagrangian strain tensor, Eulerian strain tensor

1 Introduction

Effective use of materials in engineering practice requires thorough identification of their mechanical properties, as well as a deep understanding of their behavior under various loading modes. Reliable determination of these properties forms the foundation for designing safe and functional components, optimizing manufacturing processes, and predicting the service life of materials under real-world operating conditions.

However, the accuracy and reliability of mechanical testing results depend heavily on proper execution. This includes not only the selection of an appropriate testing method—typically based on relevant standards—but also correct sample preparation, adherence to testing conditions, and careful interpretation of the collected data. The choice of a specific type of mechanical test is determined by the nature of the required material data and by the demands for accuracy, repeatability, and relevance of the measurements with respect to the intended application of the material [1–9].

Mechanical testing of materials is primarily concerned with two essential properties: strength and ductility. These characteristics are critical for assessing whether a material is suitable for a given engineering application. To achieve reliable, reproducible, and statistically valid results, it is crucial to follow clearly defined and, in most cases, standardized testing protocols. In engineering practice, internationally recognized standards are commonly used—such as ASTM D638 [10] for tensile testing of plastics, and ISO 6892-1 [11] for metallic materials. These standards outline comprehensive testing procedures, covering aspects such as specimen geometry, test conditions, equipment requirements, strain rate, data collection methods, and evaluation criteria. Consistent application of these guidelines is essential to ensure the credibility and comparability of the measured data.

To determine the fundamental mechanical properties of a material—such as strength and ductility—the focus is typically placed on measuring the applied forces and the corresponding displacements of the specimen during loading. Using these measurements, values of stress and strain, which are the primary outputs of tensile tests, can be calculated based on fundamental equations from mechanics. Displacement measurement can be carried out using a variety of technical approaches, including both contact and non-

contact methods [12]. While contact extensometers have long been the industry standard, non-contact technologies have seen rapid advancement in recent years, largely due to progress in optics, computational devices, and image processing techniques.

Modern non-contact extensometers enable accurate, fast, and non-invasive tracking of deformation without physical interaction with the specimen. This eliminates potential interference between the measuring device and the test sample, improving measurement integrity. In a previous study, the authors introduced a custom displacement measurement method based on computer vision principles [13]. This approach involved applying regions of interest—such as contrasting lines—onto the specimen's surface. The centroid positions of these regions were tracked throughout the test, and changes in their location were used to determine local displacements. The results demonstrated that this non-contact method offers sufficient accuracy, even when compared to digital image correlation (DIC), and represents a promising alternative to conventional contact-based techniques. During the review process of that study, reviewers highlighted the potential for extending the proposed method beyond the evaluation of displacements along the loading axis. They suggested that the methodology could be further enhanced by incorporating the analysis of strain components, including those occurring transverse to the loading direction.

Building on these findings, the current work extends the method toward full-field strain determination. Specifically, the study investigates the strain field of additively manufactured thermoplastic specimens produced by Fused Filament Fabrication (FFF). The experiments were conducted using specimens fabricated from polyethylene terephthalate glycol (PET-G), a commonly used thermoplastic in additive manufacturing due to its good mechanical stability and optical clarity [14-15]. Circular markers were printed directly onto the specimen surface during fabrication by FFF technology using black PET-G filament, providing high-contrast features that enable two-dimensional displacement tracking. Once the test begins, the circular markers are detected using object boundary detection algorithms, and the centroid position of each marker is tracked throughout the tensile test. The resulting trajectories are then used to calculate displacement vectors, which form the basis for constructing various strain tensors—ranging from infinitesimal linear models to geometrically nonlinear formulations, such as the Lagrangian and Eulerian strain tensors [16–17]. Strain tensors are computed for each marker and for every frame, generating a detailed temporal map of local deformations. This analysis enables not only the observation of strain evolution over time but also a comparison of different mathematical approaches and their influence on the interpretation of the resulting strain fields. The proposed approach thus aims contributes to the field of experimental

mechanics by providing an accessible and accurate optical method for strain field determination in additively manufactured thermoplastics.

2 Theoretical background

Determination of the deformation field using computer vision requires a sound understanding of both methods for displacement measurement methods, such as object boundary detection and the fundamental principles of continuum mechanics. This section provides the theoretical foundation necessary for the formulation of strain tensors, beginning with the definition of displacement, and culminating in strain measures for both small and large deformations.

2.1 Displacement gradient

The displacement vector u of any point in a deformable body can be described as:

$$u = x - X, \tag{1}$$

Where:

x...The current (deformed) position of the point, X...Original (reference) position.

By differentiating the displacement with respect to the components of *X*, we obtain the displacement gradient, which in two dimensions takes the form:

$$\nabla u = \begin{bmatrix} \frac{\partial u_1}{\partial X_1} & \frac{\partial u_1}{\partial X_2} \\ \frac{\partial u_2}{\partial X_1} & \frac{\partial u_2}{\partial X_2} \end{bmatrix}, \tag{2}$$

Where:

 u_i , X_i ...The components of the vectors u and X, respectively.

In practical applications, particularly when working with experimental or numerically generated data, the displacement field is typically defined only at discrete points. In such cases, the partial derivatives in equation (2) are approximated using finite differences:

$$\nabla u^* = \begin{bmatrix} \frac{\Delta u_1}{\Delta X_1} & \frac{\Delta u_1}{\Delta X_2} \\ \frac{\Delta u_2}{\Delta X_1} & \frac{\Delta u_2}{\Delta X_2} \end{bmatrix}, \tag{3}$$

2.2 Deformation gradient tensor

Under deformation, an infinitesimal element $d\mathbf{X}$ in the reference configuration is mapped to an element $d\mathbf{x}$ in the deformed configuration. This transformation is governed by the deformation gradient tensor F:

$$dx = FdX, (4)$$

For planar problems, the deformation gradient can be expressed as:

$$\mathbf{F} = \nabla \mathbf{x} = \mathbf{I} + \nabla u = \begin{bmatrix} \frac{\partial x_1}{\partial X_1} & \frac{\partial x_1}{\partial X_2} \\ \frac{\partial x_2}{\partial X_1} & \frac{\partial x_2}{\partial X_2} \end{bmatrix}, \tag{5}$$

Where:

I...The identity tensor,

 x_i ...The components of the current position vector x.

As with the displacement gradient, the derivatives in equation (5) can be approximated using finite differences when dealing with discrete data.

Provided that the deformation gradient tensor F is invertible, it can be decomposed into an orthogonal tensor R, representing rigid body motion, and a symmetric tensor U or V, representing pure stretch:

$$F = RU = VR, \tag{6}$$

The material deformation is characterized by the symmetric stretch tensors U and V, which serve as the basis for defining the right and left Cauchy-Green deformation tensors. These, in turn, are used to compute the Lagrangian and Eulerian strain tensors, which will be introduced in the subsequent subsections.

2.3 Infinitesimal strain tensor

The infinitesimal strain tensor E is a symmetric second-order tensor that characterizes small deformations of an elastic body relative to its undeformed, reference configuration. It is defined as the symmetric part of the displacement gradient ∇u , and is given by:

$$E = \frac{1}{2} [(\nabla u)^T + \nabla u]. \tag{7}$$

This linearized strain measure provides an adequate approximation of the deformation state only under the assumption of small strains and small displacements. In such cases, geometric nonlinearities are negligible, and the use of linear kinematic relations is justified.

However, in cases involving large deformations, the use of infinitesimal strain tensor becomes inadequate, as it fails to capture significant geometric changes. In these cases, finite strain theory is required, and the deformation must be characterized using nonlinear strain measures such as the Green-Lagrange strain tensor or the Euler-Almansi strain tensor. Finite strain theory incorporates higher-order terms and provides a more accurate representation of the deformation kinematics in large-strain regimes.

2.4 Finite strain tensors

In the presence of large deformations, it is necessary to employ nonlinear strain measures. These are formulated with respect to two primary configurations: the reference (material) configuration and the current (spatial) configuration, each associated with an appropriate deformation tensor. The corresponding deformation tensors associated with each configuration will be introduced in the following sentences.

2.4.1 Right Cauchy – Green deformation tensor

The right Cauchy-Green deformation tensor C quantifies the stretch of material elements with respect to the reference configuration. It is defined as:

$$C = U^2 = F^T F, \tag{8}$$

F...The deformation gradient tensor,

U...The right pure stretch tensor derived from the decomposition of F.

The tensor C is symmetric and positive-definite, and it plays a central role in Lagrangian (materialbased) formulations of strain.

2.4.2 Left Cauchy – Green deformation tensor

In contrast to the right Cauchy-Green tensor, which describes deformation relative to the undeformed (reference) configuration, the left Cauchy-Green deformation tensor B characterizes deformation with respect to the current (deformed) configuration. It is defined as:

$$B = V^2 = FF^T, \tag{10}$$

Where:

F...The deformation gradient tensor,

V...The left stretch tensor obtained through the decomposition of F (see Equation 6).

The tensor B is symmetric and positive-definite, which describes local strains in the spatial (Eulerian) frame. It is frequently used in continuum mechanics formulations that are based on the deformed geometry of the body.

2.4.3 Lagrangian (Green-Lagrange) Strain Ten-

The Lagrangian strain tensor E*, also known as the Green-Lagrange strain tensor, is derived directly from the right Cauchy–Green tensor C: $E^* = \frac{1}{2}(C - I),$

$$E^* = \frac{1}{2}(C - I),\tag{9}$$

Where:

I...The second-order identity tensor.

This strain measure captures the finite deformation of a material by accounting for both large displacements and rotations. Unlike the infinitesimal strain tensor, Lagrangian strain tensor E* remains valid under geometrically nonlinear conditions. In the limit of small strains and small rotations, E* converges to the linearized (infinitesimal) strain tensor E, ensuring consistency with classical small-strain theory.

2.4.4 Eulerian (Euler-Almansi) Strain Tensor

From the left Cauchy-Green deformation tensor B, the Eulerian strain tensor e*, also known as the Euler-Almansi strain tensor, is defined:

$$e^* = \frac{1}{2}(I - B^{-1}). \tag{11}$$
 This tensor provides a measure of deformation re-

lative to the current configuration and, like the Lagrangian strain tensor, is capable of capturing large deformation states.

This strain measure characterizes the deformation of a material element with respect to its current (deformed) configuration. Similar to the Green-Lagrange strain tensor E*, it is suitable for finite strain analysis, as it accounts for both large displacements and rotations. However, unlike E*, which is defined in the reference (material) configuration, e* is formulated in the spatial (Eulerian) frame, making it particularly useful in problems involving large deformations and evolving geometries.

2.5 Component Form of the Strain Tensor

In a two-dimensional plane, the components of a general strain tensor ϵ can be expressed in matrix form as:

$$\varepsilon = \begin{bmatrix} \varepsilon_{11} & \varepsilon_{12} \\ \varepsilon_{21} & \varepsilon_{22} \end{bmatrix}, \tag{12}$$

Where:

ε...Any of the strain tensors previously introduced, such as the infinitesimal strain tensor, Green–Lagrange strain tensor, or Euler–Almansi strain tensor.

The diagonal components, ε_{11} and ε_{22} , correspond to the normal strains along the X- and Y-axis, respectively, indicating elongation or compression in those directions. The off-diagonal components, ε_{12} and ε_{21} , represent shear strains in the XY and YX planes, respectively.

According to the principle of shear strain reciprocity (also known as the law of conjugate shear stresses), the shear components are equal:

$$\varepsilon_{12} = \varepsilon_{21}.\tag{13}$$

This symmetry implies that the strain tensor ε is symmetric. The symmetric nature of the strain tensor is essential in continuum mechanics, as it reflects physical consistency in the material's deformation behavior.

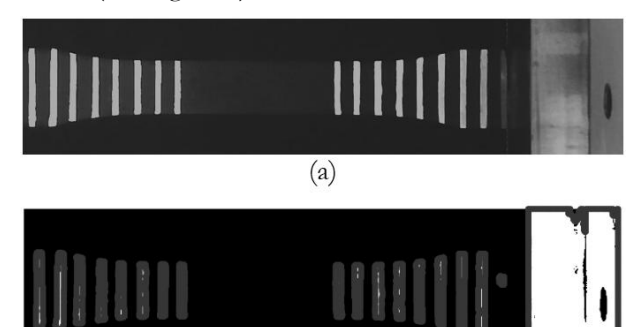
3 Experiment preparation

Displacement measurements were conducted using a non-contact extensometer based on object boundary detection. The authors previously published a detailed study presenting this approach. However, that study primarily focused on creating markers (lines) on the surface of a flat test specimen. Subsequently, an image was captured, and object boundary detection algorithms were employed to identify the boundaries of the markers and calculate the positions of their centroids. This procedure was repeated for all captured images, enabling the tracking of individual marker centroids over time and the subsequent computation of displacements.

This methodology can also be applied using alternative marker shapes, such as circles. An advantage of circular markers, compared to line markers, is their ability to capture both longitudinal and transverse displacements upon application, thereby enabling the determination of the full strain field. The measurement procedure consists of two primary steps:

- Recording the tensile test,
- Processing the recorded data through centroid detection.

The tensile test was conducted using a modified dog-bone specimen fabricated via Fused Filament Fabrication (FFF) technology. The specimen's geometry and dimensions are illustrated in Figure 2. The specimen was printed from white PET-G material [14–15]. Circular markers were produced from the black PET-G to ensure reliable detection and maximum contrast against the white background. These markers were concentrated within the waist region of the specimen (see Figure 2).



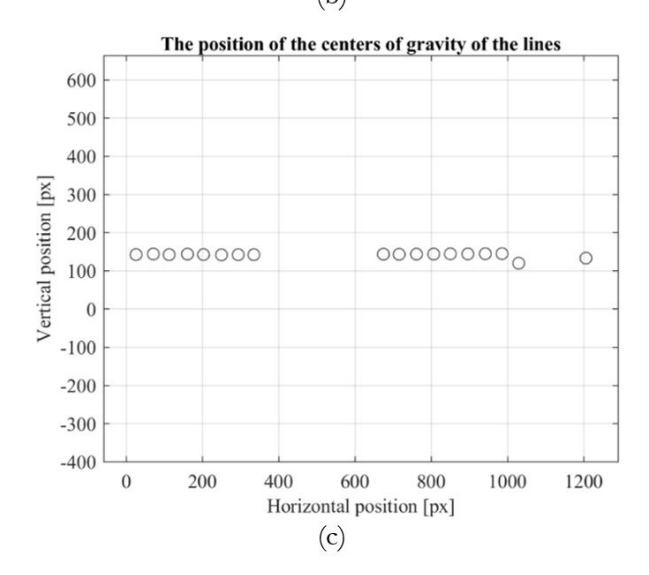


Fig. 1 Detection of the markers' centers of gravity: (a) photo of observed area, (b) objects' detection, (c) positions of the centers of gravity of all detected objects

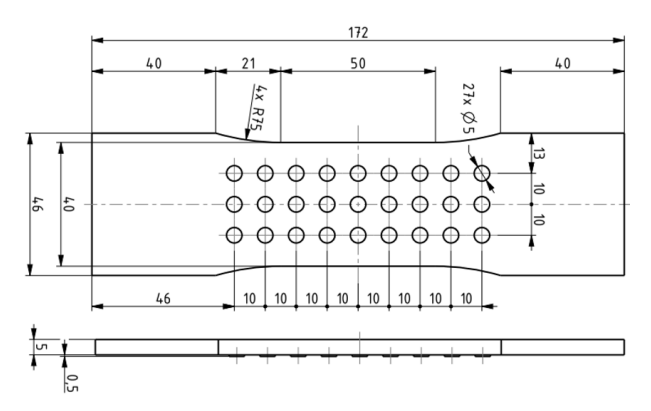


Fig. 2 Specimen dimensions

The tensile test was recorded using a Trust 4K Ultra HD webcam [18] with a resolution of 3840×2160 pixels. To ensure accurate and reliable displacement measurements, the fundamental imaging conditions were carefully maintained: the camera was positioned parallel to the specimen surface, manual focus was applied to avoid automatic adjustments, and the camerato-specimen distance was optimized for maximum clarity and contrast.

Image acquisition was performed at a frequency of one frame every 0.5 seconds. The entire recording process was automated using a custom MATLAB script. An illustration of the experimental setup is provided in Figure X.

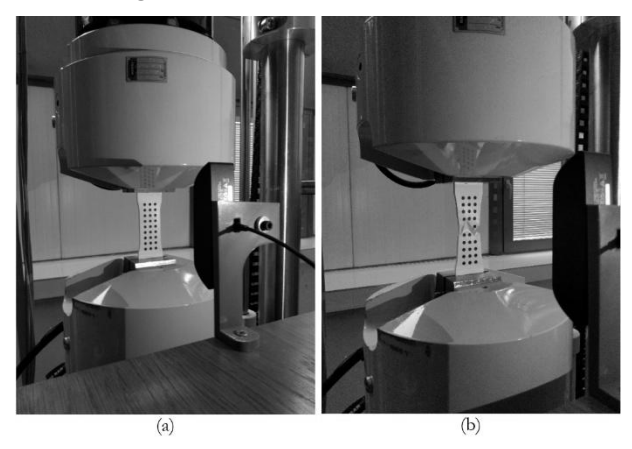


Fig. 3 The measurement process: (a) start of the measurement, (b) end of the measurement

Following the image acquisition phase, the recorded image sequence was processed to extract displacement data. This stage consisted of three primary steps:

- Detection of the centroids of circular markers,
- Computation of marker displacements over time,
- Construction of the deformation field.

The centroid detection was carried out using MATLAB. The core methodology followed the approach described in study [13]. However, due to the use of circular rather than linear markers, the image processing pipeline required specific adjustments.

The regionprops function in MATLAB was employed for marker analysis [19], with the properties Centroid, MajorAxisLength, and MinorAxisLength selected as output parameters. The Centroid parameter directly provides the coordinates of the geometric center of each detected object. The remaining parameters correspond to the lengths of the major and minor axes of the best-fit ellipse for each region, which are especially relevant when circular objects may appear slightly distorted due to perspective or image resolution.

These measurements were further used to estimate the radius r of each circular marker by applying the relationship:

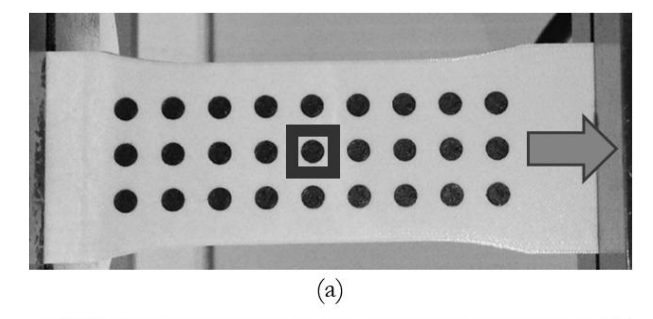
 $r = \frac{A+a}{4} \tag{14}$

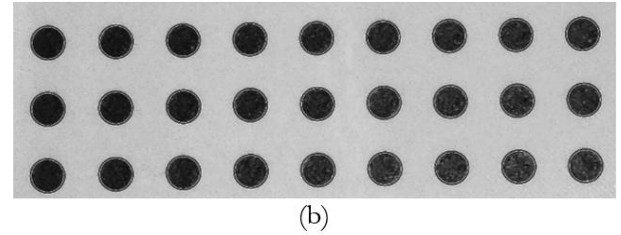
Where:

A, a...The lengths of the major and minor axes, respectively.

This information enabled consistency checks on marker size and contributed to robust tracking across frames.

Fig. 4(a) shows the test specimen clamped in the jaws of the testing machine, with the green arrow indicating the direction of loading. The circular markers were successfully detected, and their boundaries were highlighted in red, as illustrated in Fig. 4(b). Based on prior experience, reducing the detection area significantly improves both the accuracy of centroid detection and the speed of the image processing. The final output of this procedure is the position of the centroids of the individual circular markers (Fig. 4c).





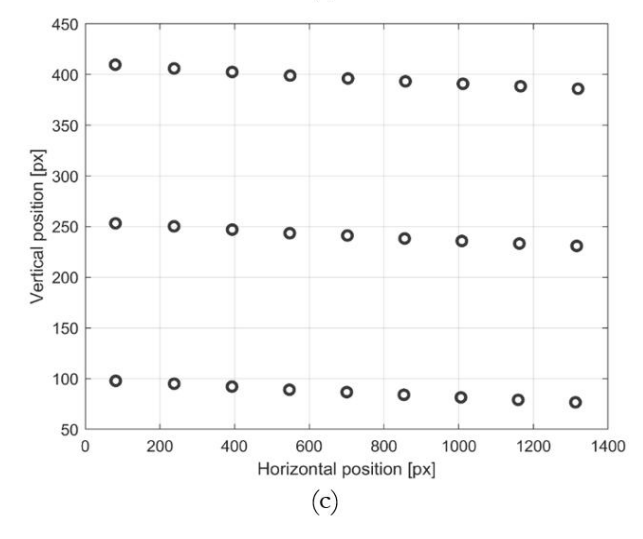


Fig. 4 Detection of circular marker centroids: (a) overview of the detection region, (b) visualization of detected circles in the cropped region, (c) position of centroids of all detected circles

4 Results

After completing the measurement, the evaluation of the recorded data can proceed. The output consists of a matrix representing the positions of individual centroids over time, i.e., across successive frames. A total of 130 frames were captured, resulting in 130 (X, Y) coordinates for each marker. However, only the first 105 frames were analyzed. This decision was based on the observation that the specimen was already damaged. Since the material had failed, further measurements would no longer yield meaningful information for determining the deformation field.

The authors constructed three strain tensors for each marker:

• The infinitesimal strain tensor E,

• The Eulerian strain tensor e*.

The Lagrangian strain tensor E*,

Figure 5 presents the temporal evolution of strain for the central marker, highlighted by the red rectangle in Figure 4(a). The corresponding graphs depict the individual components of the strain tensors, with subscript notation matching the tensor components defined in Equation 12.

Assuming small deformations within the elastic region of the material, all three formulations yield equivalent results, as can be observed in Figure 5 up to approximately 20 seconds. Additionally, the behavior of the shear strain components demonstrates compliance with the law of complementary shear stresses.

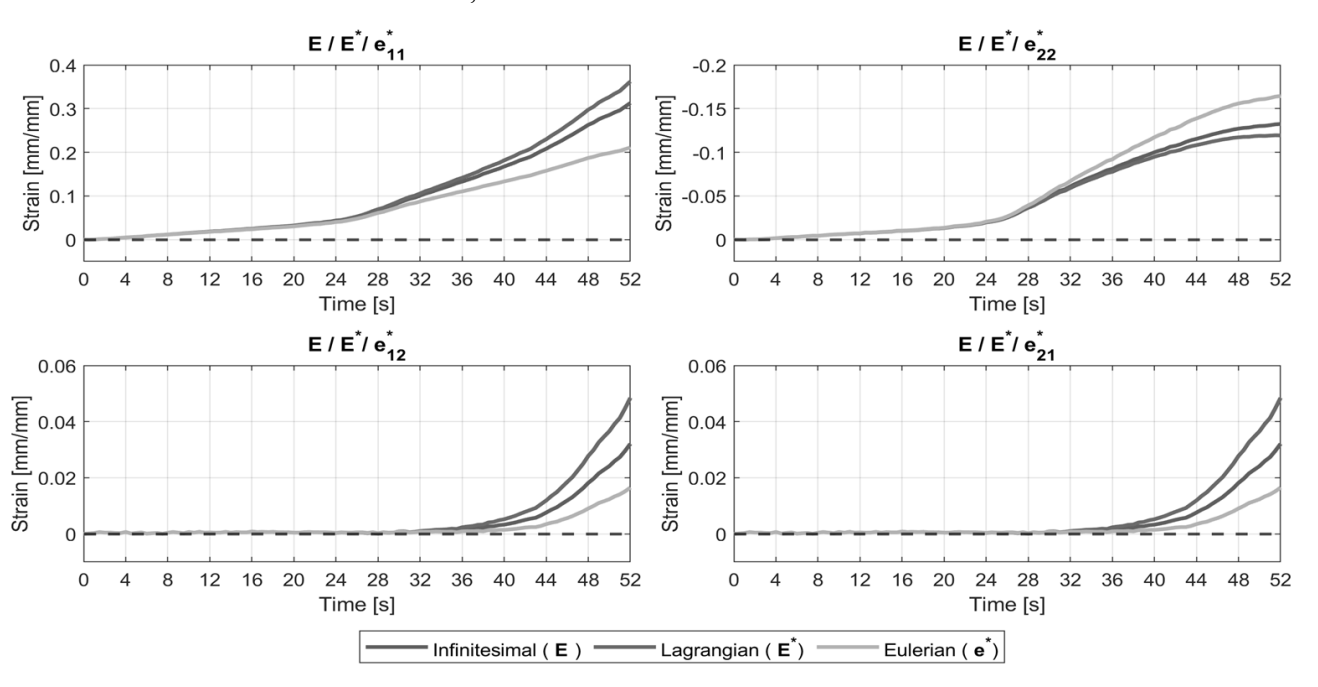


Fig. 5 The time-dependent behavior of the individual strain tensor components

For the observed markers shown in Fig. 4b, interpolation allows the deformation fields to be visualized in different directions—along the loading direction, perpendicular to it, and also for the shear components of strain. The deformation fields in the loading direction (component ϵ_{11}) for the selected types of strain tensors (E, E*, e*) are presented in Fig. 6.

Figure 6 (left) displays the infinitesimal strain field (E₁₁). The region of highest strains is located in the central part of the observed sample area. In this region, the calculated strain slightly exceeds a value of 0.3. Under such conditions, this approach is no longer suitable for strain evaluation, as the maximum absolute strain surpasses the 2% threshold, beyond which the deformation can no longer be considered small and the use of linear theory becomes invalid.

The center image in Figure 6 shows the Lagrangian strain field (E_{11}^*) . Similar to the infinitesimal strain

field, the highest strain values are again found in the central region of the sample. However, the strain values are even higher, exceeding 0.36. This increase is due to the fact that the infinitesimal approach neglects higher-order terms in the strain tensor components, which are included in the Lagrangian formulation.

Figure 6 (right) presents the Eulerian strain field (e_{11}^*) . The area of maximum deformation is likewise located in the central region of the sample. However, in this case, the strain values are the lowest, with a maximum close to 0.21. This reduction is a result of the Eulerian formulation expressing deformation relative to the current (deformed) configuration, in contrast to the previous approaches, which refer to the original (undeformed) configuration. Since tensile loading causes elongation and thus an increase in the current length, the resulting strain values are reduced accordingly.

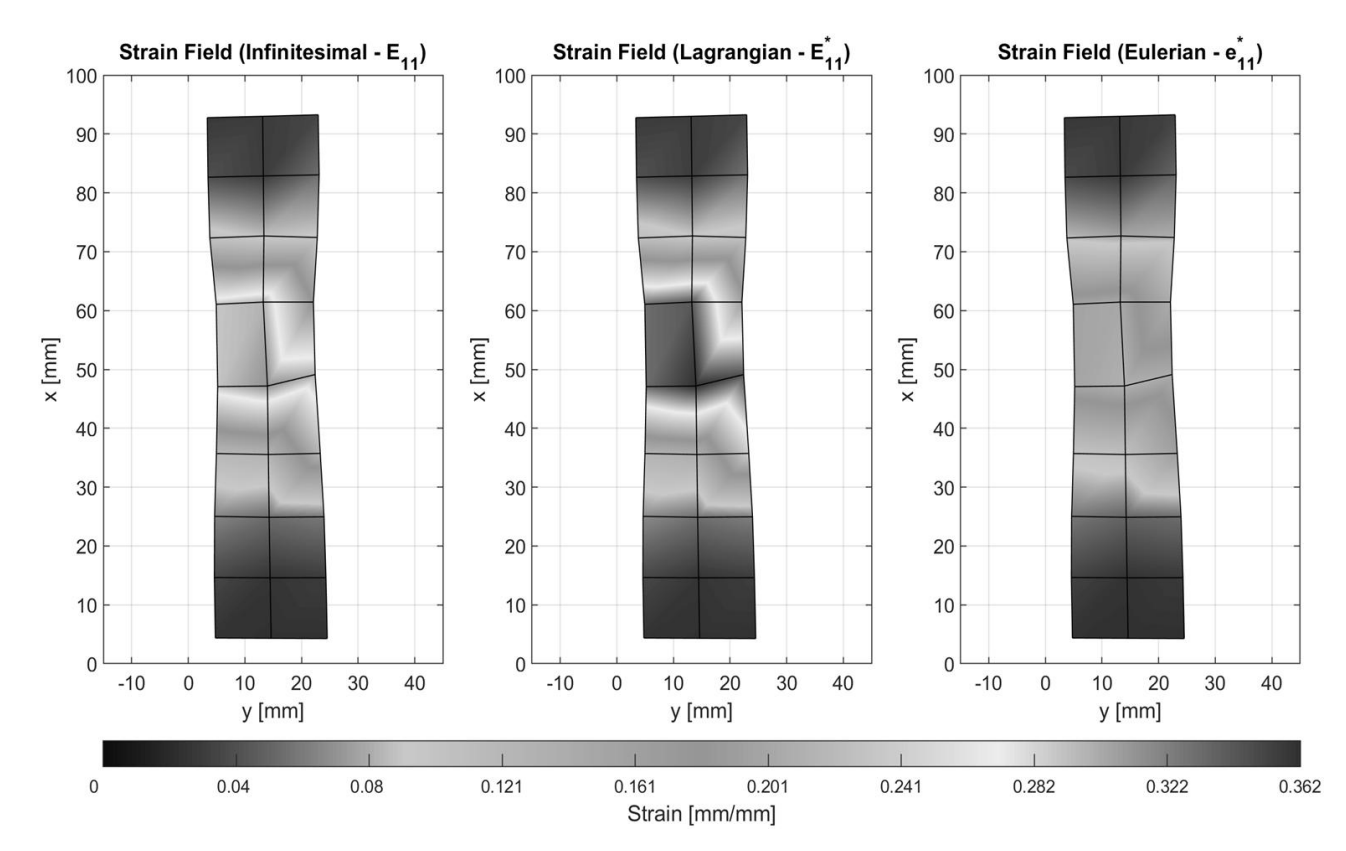


Fig. 6 Selected types of strain fields oriented in the loading direction: left — Infinitesimal strain field E, middle — Lagrangian strain field e*

Figure 7 shows the deformation fields oriented perpendicularly to the loading direction (ϵ_{22}). As indicated by the color legend below the deformation

maps, the sample undergoes contraction in this direction, which corresponds to negative strain values.

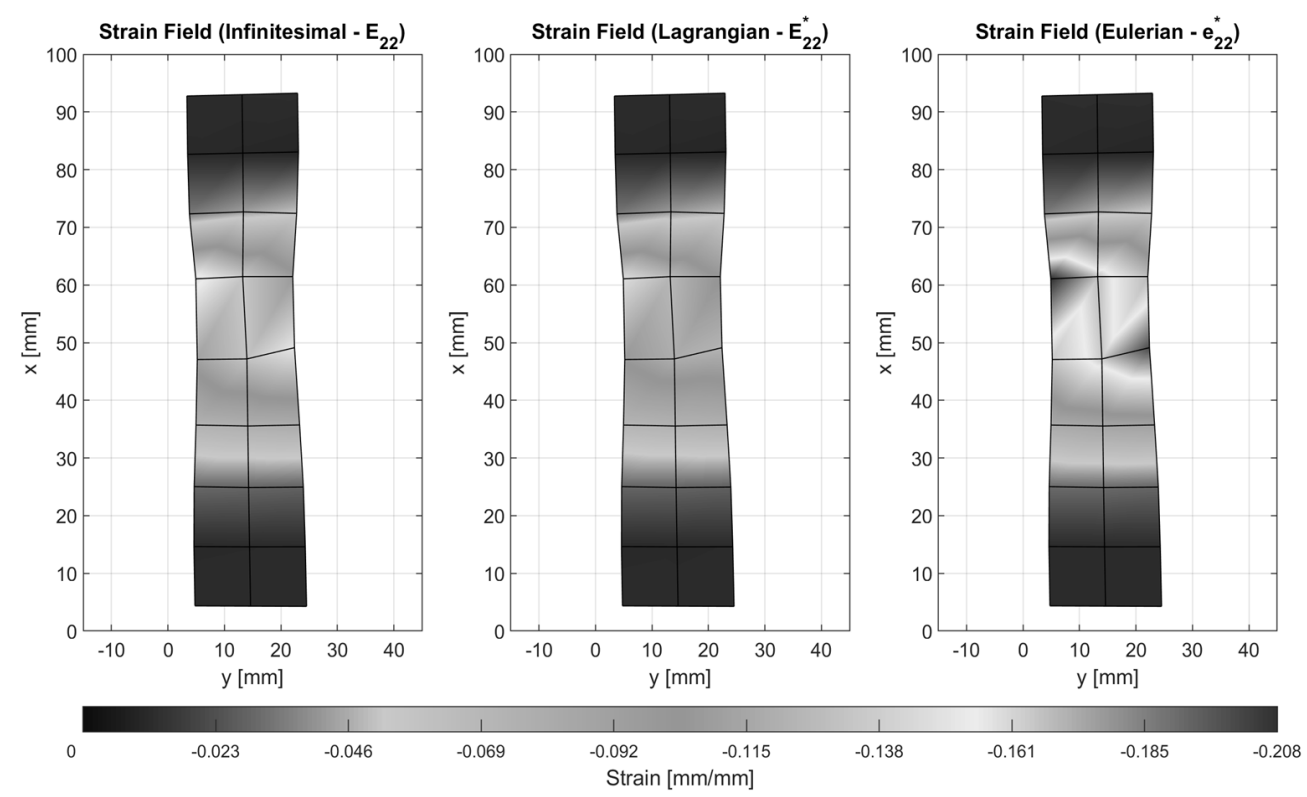


Fig. 7 Selected types of strain fields oriented perpendicularly to the loading direction: left — Infinitesimal strain field E, middle — Lagrangian strain field E*, right — Eulerian strain field e*

Figure 7 (left) presents the infinitesimal strain field (E₂₂). The region of greatest transverse contraction, reaching value -0.16, is located in the central part of the specimen, similar to the strain distribution oriented in the loading direction. However, due to the high absolute strain value, the use of the infinitesimal approach is once again inappropriate, as the assumption of small deformations is violated.

The center image displays the Lagrangian strain field (E_{22}^*). The maximum contraction value, approximately -0.15, also occurs in the central region. In this case, the Lagrangian approach yields the lowest absolute strain values. Nevertheless, these values remain algebraically greater than those obtained using the infinitesimal strain theory.

The right image in Figure 7 shows the Eulerian strain field (e_{22}^*). In this case, the maximum transverse contraction approaches -0.21. This formulation yields the highest absolute strain values, although they are algebraically the smallest. This outcome is again related to the fact that the Eulerian approach evaluates deformation relative to the current (deformed) configuration. As the specimen continuously narrows in the transverse direction, the ratio of dimensional change to the decreasing actual size leads to a greater absolute value of strain.

Figure 8 shows the shear strain fields ($\epsilon_{12}=\epsilon_{21}$). As indicated by the color legend beneath the deformation maps, both positive and negative shear strain values are present, corresponding to shearing in different directions. However, in this case, the dominant shear deformations are positive.

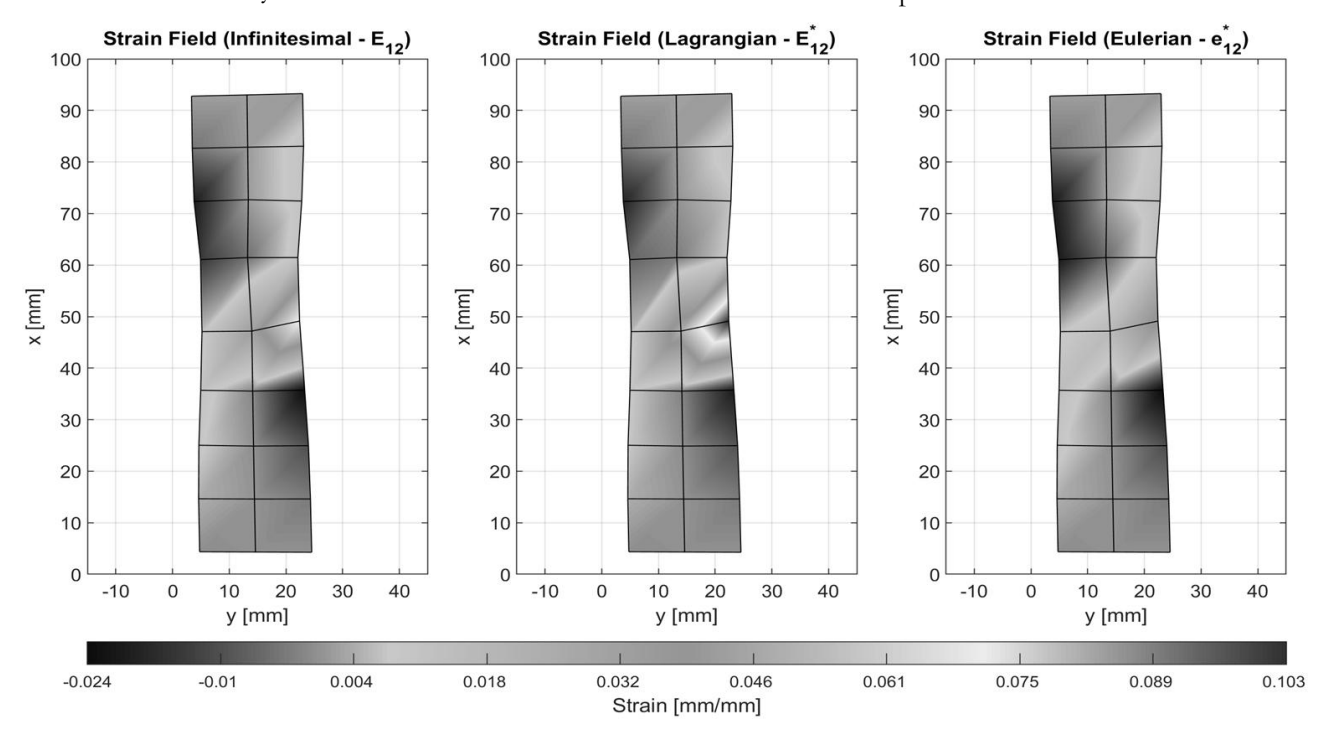


Fig. 8 Selected types of shear strain fields: left — Infinitesimal strain field E, middle — Lagrangian strain field E*, right — Eulerian strain field e*

Figure 8 (left) displays the infinitesimal strain field (E_{12}) . The region with the highest shear strain, approximately 0.07, is again located in the central part of the specimen. However, as the strain values exceed the range of small deformations, the use of this approach is considered inappropriate.

The center image shows the Lagrangian strain field (E_{12}^*) . The maximum shear strain of about 0.1 is also concentrated in the specimen's central region. It is evident from the figure that the Lagrangian approach yields the highest absolute shear strain values.

The right image presents the Eulerian strain field (e_{12}^*) . Here, the maximum shear strain reaches approximately 0.04, representing the lowest absolute shear strain values among the three approaches.

5 Conclusion

The aim of this paper was to present a method for determining the strain field of additively manufactured thermoplastics using computer vision techniques. The proposed approach enables non-contact measurement of displacements by detecting the centroids of circular markers applied to the test specimen. Since the flat specimen was fabricated via 3D printing using Fused Filament Fabrication technology, the markers were produced using the same method. The authors conducted a tensile test recorded with a webcam. Recording the test enables reproducible evaluation of displacements. Through image analysis, the positions of the centroids of all markers were successfully detected across every frame.

Based on the obtained centroid positions, displacements were derived and used to construct selected strain tensors - infinitesimal, Lagrangian, and Eulerian strain tensors - for all markers. The authors provided a detailed description of the tensors for a selected marker. Comparison of results showed that the infinitesimal strain tensor describes the specimen's deformation state comparably to the Lagrangian and Eulerian strain tensors only for small displacements and strains. The infinitesimal strain tensor represents a simplified model that does not yield sufficiently accurate results for large displacements. This limitation is documented by progressively increasing discrepancies observed once the material's linear elastic range is exceeded. Both the Lagrangian and Eulerian strain tensors adequately characterize large deformation states. However, these approaches differ in their reference geometry for evaluating material deformation. The Lagrangian strain tensor captures large deformations relative to the specimen's original (undeformed) geometry or monitored area, whereas the Eulerian strain tensor assesses deformations relative to the current (deformed) geometry. This distinction leads to differing strain values, particularly under large deformations. The most pronounced differences between the approaches were observed in transverse and shear strain components.

The obtained strain fields for the individual tensor components demonstrated the proposed method's capability to reliably and efficiently capture and describe the distribution of strains in a plane. This approach holds significant potential for applications in characterizing the mechanical behavior not only of 3D-printed polymers but also of 3D-printed composites, conventionally manufactured composites, and metallic materials.

Future research will focus on exploring more suitable methods for accurately describing the displacement field, which is essential for the subsequent calculation of the strain field. Among the considered approaches is the creation of a finite element mesh connecting the centroids of individual markers. Alternatively, the structured marker arrays could be replaced by a points cloud, where discrete displacement values at these points could be interpolated using various methods, such as polynomial surfaces, interpolation, or regression techniques. These approaches have the potential to improve the accuracy of differential calculations and, in some cases, allow for direct utilization of displacement field derivatives. This, in turn, may lead to higher precision and smoother strain distributions within the computational model.

Acknowledgement

This research was funded by the EU NextGenerationEU through the Recovery and Resilience Plan for Slovakia under the project No. 09103-03-

V05-00002. Additional support was provided by project KEGA no. 005ŽU-4/2024.

References

- [1] MAJKO, J., VAŠKO, M., HANDRIK, M., SÁGA, M. (2022). Tensile Properties of Additively Manufactured Thermoplastic Composites Reinforced with Chopped Carbon Fibre. In: *Materials*, Vol. 15, No. 1. MDPI. https://doi.org/10.3390/ma15124224
- [2] VAŠKO, M., SÁGA, M., MAJKO, J., VAŠKO, A., HANDRIK, M. (2020). Impact Toughness of FRTP Composites Produced by 3D Printing. In: *Materials*, Vol. 13, No. 24. MDPI. https://doi.org/10.3390/ma13245654
- [3] ŠOFER, M., CIENCIALA, J., ŠOFER, P., PAŠKA, Z., FOJTÍK, F., FUSEK, M., CZERNEK, P. (2024). Transverse Cracking Signal Characterization in CFRP Laminates Using Modal Acoustic Emission and Digital Image Correlation Techniques. In: *Composites Science and Technology*, Vol. 255. Elsevier. https://doi.org/10.1016/j.compscitech.2024.110697
- [4] RAO, J., SING, S. L., LIU, P., WANG, J., SOHN, H. (2023). Non-destructive Testing of Metal-based Additively Manufactured Parts and Processes: A Review. In: Virtual and Physical Prototyping, Vol. 18, No. 1. Taylor & Francis. https://doi.org/10.1080/17452759.2023.2266 658
- [5] DRVÁROVÁ, B., DEGANOVÁ, L., NOVÁK, P., ZAPOMNĚL, J., DEKÝŠ, V. (2024). Comparison of Dissipation Energy in PLA, ABS and PETG Materials Used in 3D Printing. In: Acta Physica Polonica A, Vol. 146, No. 6, pp. 810–813. Polish Academy of Sciences. https://doi.org/10.12693/APhys-PolA.146.810
- [6] FALES, A., ČERNOHLÁVEK, V., SUSZYNSKI, M., ŠTĚRBA, J., ZDRÁHAL, T., NOCAR, D. (2025). Experimental Measurement and Testing of 3D Printed Parts in Terms of the Material Used. In: *Manufacturing Technology*, Vol. 25, No. 2, pp. 174–184. UJEP. DOI: 10.21062/mft.2025.016
- [7] JIN, F., LU, W., AN, X., ZHU, H., WANG, J. (2024). Mechanical Properties and Compression Performance of 3D Printed HIPS Polymer Lattice Structure. In: *Manufacturing Technology*, Vol. 24, No. 3, pp. 378–392. UJEP. DOI: 10.21062/mft.2024.054

- [8] VARHANIK, M., SEDLAK, J., STUDENY, Z., JANIGOVA, P., CHROMJAKOVA, F. (2024). Tribological Properties of 3D Printed Materials in Total Knee Endoprosthesis. In: *Manufacturing Technology*, Vol. 24, No. 2, pp. 294– 306. UJEP. DOI: 10.21062/mft.2024.032
- [9] SAPIETA, M., DEKÝŠ, V., KACO, M., PÁSTOR, M., SAPIETOVÁ, A., DRVÁROVÁ, B. (2023). Investigation of the Mechanical Properties of Spur Involute Gearing by Infrared Thermography. In: Applied Sciences, Vol. 13, No. 10. MDPI. https://doi.org/10.3390/app13105988
- [10] ASTM D638-14. Standard Test Method for Tensile Properties of Plastics .ASTM International. West Conshohocken, PA: s.n., 2022
- [11] ISO 6892-1: 2019 Metallic materials Tensile testing. ISO. Geneva. Switzerland: s.n., 2019
- [12] TIAN, Q. H., YAN, L. P., YANG, T., CHEN, B. Y. (2011). Recent Developments of Material Deformation Measurement. In: Applied Mechanics and Materials, Vols. 117–119, pp. 122–128. Trans Tech Publications. https://doi.org/10.4028/www.scientific.net/AMM.117-119.122
- [13] PIROH, O., MAJKO, J., HANDRIK, M., VAŠKO, M., CIENCIALA, J., ŠOFER, M., FUSEK, M., SÁGA, M. (2025). Rapid and Cost-efficient Approach for Non-contact Mea-

- surement in Experimental Mechanics. In: *Results in Engineering*, Vol. 26. Elsevier. https://doi.org/10.1016/j.rineng.2025.105408
- [14] LAKSHMAN, SRI S. V., KARTHICK, A., DINESH, C. (2024). Evaluation of Mechanical Properties of 3D Printed PETG and Polyamide (6) Polymers. In: *Chemical Physics Impact*, Vol. 8. Elsevier. https://doi.org/10.1016/j.chphi.2024.100491
- [15] DOLZYK, G., JUNG, S. (2019). Tensile and Fatigue Analysis of 3D-Printed Polyethylene Terephthalate Glycol. In: *Journal of Failure Analysis and Prevention*, Vol. 19, pp. 511–518. Springer. https://doi.org/10.1007/s11668-019-00631-z
- [16] LAI, W. M., RUBIN, D., KREMPL, E. (1993).
 Introduction to Continuum Mechanics, pp. 1–
 X. Butterworth-Heinemann Ltd., Oxford.
 ISBN 0750628944.
- [17] REDDY, J. N. (2013). An Introduction to Continuum Mechanics, Second Edition, pp. 1–X. Cambridge University Press, Cambridge. ISBN 9781107025431.
- [18] Trust. Trust Teza 4K Ultra HD Webcam. Available at: https://www.trust.com/en/product/24280-teza-4k-ultra-hd-webcam (Accessed 20th June 2025).
- [19] MathWorks. regionprops. Available at: https://www.mathworks.com/help/images/r ef/regionprops.html, (Accessed 20th June 2025).